Atmos. Meas. Tech., 7, 581–597, 2014
www.atmos-meas-tech.net/7/581/2014/
doi:10.5194/amt-7-581-2014

Atmospheric Measurement Techniques
Open Access

The identification and tracking of volcanic ash using the Meteosat Second Generation (MSG) Spinning Enhanced Visible and Infrared Imager (SEVIRI)

A. R. Naeger[1] **and S. A. Christopher**[1,2]

[1]Department of Atmospheric Sciences, UAHuntsville, 320 Sparkman Drive Huntsville, AL 35805, USA
[2]Earth System Science Center, UAHuntsville, 320 Sparkman Drive Huntsville, AL 35805, USA

Correspondence to: A. R. Naeger (naeger@nsstc.uah.edu)

Received: 10 May 2013 – Published in Atmos. Meas. Tech. Discuss.: 21 June 2013
Revised: 14 January 2014 – Accepted: 16 January 2014 – Published: 20 February 2014

Abstract. In this paper, we develop an algorithm based on combining spectral, spatial, and temporal thresholds from the geostationary Spinning Enhanced Visible and Infrared Imager (SEVIRI) daytime measurements to identify and track different aerosol types, primarily volcanic ash. Contemporary methods typically do not use temporal information to identify ash. We focus not only on the identification and tracking of volcanic ash during the Eyjafjallajökull volcanic eruption period beginning in 14 April and ending 17 May 2010 but also on a pixel-level classification method for separating various classes in the SEVIRI images. Three case studies on 13, 16, and 17 May are analyzed in extensive detail with other satellite data including from the Moderate Resolution Imaging Spectroradiometer (MODIS), Multiangle Imaging Spectroradiometer (MISR), and Facility for Airborne Atmospheric Measurements (FAAM) BAe146 aircraft data to verify the aerosol spatial distribution maps generated by the SEVIRI algorithm. Our results indicate that the SEVIRI algorithm is able to track volcanic ash when the solar zenith angle is lower than about 65°. Furthermore, the BAe146 aircraft data show that the SEVIRI algorithm detects nearly all ash regions when AOD > 0.2. However, the algorithm has higher uncertainties when AOD is < 0.1 over water and AOD < 0.2 over land. The ash spatial distributions provided by this algorithm can be used as a critical input and validation for atmospheric dispersion models simulated by Volcanic Ash Advisory Centers (VAACs). Identifying volcanic ash is an important first step before quantitative retrievals of ash concentration can be made.

1 Introduction

The Eyjafjallajökull volcano located on the southern coast of Iceland (63.6° N, 19.6° W) began emitting ash into the atmosphere on 14 April 2010. Although only a mid-size eruption (Gudmundsson et al., 2013), the volcano had a tremendous impact on air traffic as the strong atmospheric winds transported the ash southeasterly towards Europe (Ansmann et al., 2010). By 16 April 2010, an ash plume was observed across central Europe by Aerosol Robotic Network (AERONET) sun photometers and ground-based lidars (Ansmann et al., 2011). The presence of ash caused nearly a week-long stoppage in air travel over many parts of Europe since volcanic ash can have damaging effects on commercial airplanes (Casadevall, 1992). Flight cancellations that occurred over the ensuing week proved extremely costly to the airline industry as monetary losses were over USD 1 billion (Christopher et al., 2012). Therefore, it is critical that we accurately track volcanic ash during an eruption period.

To track the spatial distribution of volcanic ash, satellite remote sensing is important as the spatial distribution of ash varies strongly especially after an eruption. Ground-based stations are inadequate for understanding the spatial distribution as they only provide point measurements. Satellites are also an important tool for verifying models that predict ash concentrations and spatial distributions (Millington et al., 2012). These models are usually high-resolution dispersion models that predict height-dependent ash concentrations used by Volcanic Ash Advisory Centers (VAACs). Although polar orbiting satellites such as the Moderate Resolution Imaging Spectroradiometer (MODIS) can provide high

spatial resolution for volcanic ash plumes (Sigmundsson et al., 2010), their temporal resolution is insufficient to track ash plumes being transported long distances over relatively short timescales. Thus, geostationary satellite sensors such as the Spinning Enhanced Visible and Infrared Imager (SEVIRI) are critical for assessing the spatial distributions of ash due to their high temporal resolutions (Prata and Kerkmann, 2007; Christopher et al., 2012).

Ultimately it is important to know the vertical distribution of ash concentrations before important decisions can be made regarding commercial flights during eruptions. However the first task is to detect the volcanic ash on a pixel-by-pixel basis. The first limitation to note is that SEVIRI cannot detect ash below thick clouds, which is a common issue for passive satellite data sets that operate in the visible to the infrared part of the electromagnetic spectrum. However the repeated temporal information and the large spatial coverage make SEVIRI an excellent tool for understanding the spatial distribution of volcanic ash over large areas. One common method is to simply assign separate channels to the red, green, and blue and visually examine the ash by looking for certain colors. This is often problematic since clouds can be confused as ash and not all aerosols appear to have the same color; therefore, it is important to develop an algorithm that separates an image into various classes, such as cloud and aerosol, for further studies that may involve calculation of ash concentrations.

Prata (1989) presented a very commonly used technique that exploits the brightness temperature difference (BTD) between the 11 and 12 µm channels (BTD 11–12). The limitations with this simple technique are well known and discussed in Prata et al. (2001), where one major limitation is that high water vapor amounts can mask the negative BTD signal that the technique relies on for ash detection. However, Prata and Prata (2012) help mitigate this major limitation of the BTD 11–12 technique by including a water vapor correction term. The aircraft data used to validate their method suggest that mass loadings as low as $0.2\ \mathrm{g\ m^{-2}}$ could be detected very reliably. Pergola et al. (2004) developed a sophisticated ash detection technique that compares a measured satellite signal to a reference field computed from long-term historical records. In particular, they use three channels centered at approximately 3.75, 11.0, and 12.0 µm from the Advanced Very High Resolution Radiometer (AVHRR) to compute the reference fields and they show that this robust AVHRR technique (RAT) is more accurate in detecting volcanic ash than the simple BTD technique presented in Prata (1989). However, this approach requires multiple years of data over a region to compute the reference fields. Pavolonis et al. (2006) developed a four-channel ash detection algorithm that utilizes the 0.65, 3.75, 11.0, and 12.0 µm channels and does not rely on a reference field but instead uses spectral tests and a spatial filtering routine. They showed that this four-channel algorithm is better at detecting volcanic ash regions compared to the BTD approach, with fewer false detections. We take a different approach by developing an algorithm using SEVIRI measurements that exploits temporal thresholds along with spectral and spatial thresholds in order to classify each pixel into various classes (e.g., cloud, land, and aerosol). This algorithm uses seven different SEVIRI channels to produce detailed spatial distribution maps of cloud and aerosol.

Although the SEVIRI instrument is not equipped with near-ultraviolet (UV) channels, it is important to note the ability of the near-UV channels in detecting volcanic ash. Seftor et al. (1997) used the near-UV channels of 340 and 380 nm from the Total Ozone Mapping Spectrometer (TOMS) instrument to detect volcanic ash during the El Chichon eruption in 1982. They found that TOMS was able to successfully detect and track the ash plume even in regions where AVHRR failed to detect it, such as when a minimal temperature difference existed between the ash and surface. This is an important advantage of using the near-UV channels, as detection techniques using channels from the visible to infrared spectrums, such as the RAT and our SEVIRI algorithm, do not possess the same capability of detecting ash over snow/ice or above clouds (Pergola et al., 2004). In addition, Krotkov et al. (1999) showed that the near-UV channels of the TOMS instrument can detect the optically opaque, very fresh ash that is often missed by the visible and infrared techniques.

This study tracks the ash plumes emitted from the Eyjafjallajökull volcano from its initial eruption on 14 April until the end of the eruption period on 23 May using the high-temporal-resolution measurements of SEVIRI onboard the Meteosat Second Generation (MSG-2) satellite. Since we use the visible along with the infrared channels of SEVIRI, the algorithm developed in this study can only track the ash plumes during the daylight periods for volcanic ash in cloud-free conditions. We present results from the SEVIRI algorithm throughout the eruption period but place special emphasis on six days in May 2010 when the Facility for Airborne Atmospheric Measurements (FAAM) BAe146 research aircraft measurements were available (Johnson et al., 2012). We use the FAAM BAe146 aircraft measurements as validation for the SEVIRI algorithm developed in this study. Other sources of verification data used in this study to assess the spatial distribution of the aerosols detected by the SEVIRI algorithm include data from MODIS and the Multi-angle Imaging SpectroRadiometer (MISR).

2 Data

The goal of the paper is to develop a pixel-level algorithm from SEVIRI reflectance and temperature measurements using temporal threshold tests along with spatial and spectral threshold tests. It is important to note that the retrieval of ash concentrations and aerosol particle size information is beyond the scope of this study. We have already noted that the use of temporal thresholds and some of the spatial

Table 1. SEVIRI channels with the center, minimum, and maximum wavelengths; the channels used in the SEVIRI algorithm are highlighted in bold.

Channel	Center (μm)	Min (μm)	Max (μm)
1	**0.635**	**0.56**	**0.71**
2	0.81	0.74	0.88
3	**1.64**	**1.5**	**1.78**
4	3.9	3.48	4.36
5	6.25	5.35	7.15
6	7.35	6.85	7.85
7	**8.7**	**8.3**	**9.1**
8	9.66	9.38	9.94
9	**10.8**	**9.8**	**11.8**
10	**12**	**11**	**13**
11	13.4	12.4	14.4

thresholds used in this paper is not routinely done by standard algorithms (i.e., Prata, 1989). After classifying the volcanic ash pixels, we need to determine the accuracy of the algorithm; however this is a difficult task to accomplish. We have chosen to intercompare the SEVIRI algorithm results with MODIS and MISR products by making the assumption that their identification is correct. We take this a step further by comparing our results with aircraft data, but not many data points can be obtained with such a comparison. This is not a unique problem to our study since all validation methods have to use a verification source and then provide results and analysis.

Table 1 shows the SEVIRI channels with the center, minimum, and maximum wavelengths for each channel. These channels have a sampling distance of 3 km at sub-satellite point (Schmetz et al., 2002). The channels used to develop the SEVIRI algorithm are shown in bold, where we use two channels in the solar spectrum and three channels in the infrared spectrum.

The MODIS onboard the Terra and Aqua polar orbiter satellites have 36 channels over the spectral range from 0.4 to 14.4 μm with spatial resolutions of 250 m, 500 m, and 1 km (Savtchenko et al., 2004). A level 2 aerosol optical thickness (AOT) operational product over both ocean and non-bright land surfaces is provided by MODIS at a spatial resolution of 10 km (at nadir) by comparing measured reflectances to a lookup table of computed reflectances from a radiative transfer model (Remer et al., 2005). The reported uncertainties over ocean and non-bright surfaces are $\pm 0.03 \pm 0.05\tau$ and $\pm 0.05 \pm 0.15\tau$, respectively, where τ is aerosol optical depth (AOD) or AOT (Remer et al., 2005). Additionally, the MODIS Deep Blue algorithm provides AOT values over deserts and other bright surfaces where the reported uncertainties are approximately 20–30 % (Hsu et al., 2006). The MISR instrument onboard the Terra satellite measures upwelling shortwave radiance in four spectral channels (446, 558, 672, and 867 nm) with nine view angles and spatial resolutions of about 250 m to 1.1 km. To produce the MISR level 2 product (MIL2SAE, F12, 22) with a spatial resolution of 17.6 km, top-of-atmosphere radiances from 16×16 pixel areas of 1.1 km resolution are analyzed (Diner et al. (1999). The multispectral and multiangle instrument retrieves accurate AOT values, even over bright deserts (Christopher and Wang, 2004; Kahn et al., 2005), with expected uncertainties of ± 0.05 for AOT < 0.5 and ± 10 % for AOT > 0.5 (Martonchik et al., 1998). We use the aerosol spatial distribution from MODIS and MISR to help verify the SEVIRI results that we have developed in this paper.

A valuable validation data set used in this study is from the FAAM BAe146 research aircraft data that retrieve detailed volcanic ash measurements from the Leosphere 355 nm lidar, the Passive Cavity Aerosol Spectrometer Probe (PCASP), and the Cloud and Aerosol Spectrometer (CAS) (Marenco et al., 2011). The FAAM BAe146 aircraft flew on six days in May 2010, and aerosol extinction and AOTs at 355 nm were retrieved along with ash mass concentrations and size distributions (Marenco et al., 2011). This study focuses on 16 May and 17 May since the volcanic ash was associated with higher AOTs on these days. We utilized the AOT measurements at 355 nm retrieved from the lidar, which samples the atmosphere from 2 km above the surface to 300 m below the aircraft. Thus, the lidar AOTs exclude any boundary layer contribution except for the 17 May case, where boundary layer aerosols contribute less than 0.05 to the AOT. After integrating the AOT measurements over every minute, each retrieved AOT value corresponded to an along-track distance of 8–10 km. Note that AOT can still be derived in the presence of clouds by using the instruments onboard the BAe146 aircraft to detect and mask the cloud-contaminated areas in the vertical column of air beneath the aircraft. The usefulness of BAe146 aircraft measurements has been shown in a number of papers where the aircraft measurements were analyzed along with satellite measurements (Johnson et al., 2012; Christopher et al., 2009; Naeger et al., 2013).

3 Methodology

There is a rich heritage of classification algorithms, with the most common ones using the concept of spectral signatures where, for example, clouds "look different" based on spectral signatures in some wavelengths when compared to aerosols and land. A paper by Saunders and Kriebel (1988) used spectral and some spatial signatures to separate pixels into cloud-free, partly cloudy, or overcast scenes. Using spectral thresholds alone can cause uncertainties in image classification since there could be spectral overlap between and among classes. Thus, it is not possible to accurately separate various classes based on limited information from spectral signatures alone (Ackerman et al., 2008). For example, Fig. 1 is a SEVIRI RGB image on 17 May 2010

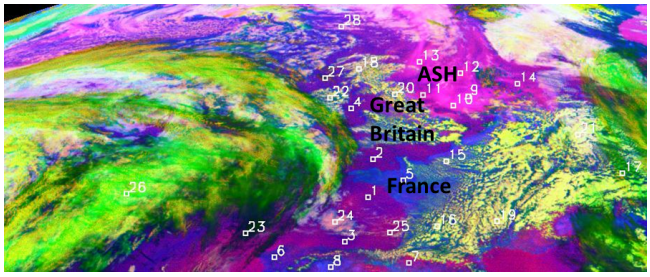

Fig. 1. SEVIRI RGB image (see the text for details) on 17 May 2010 at 13:30 UTC over Europe and the Atlantic Ocean; the 28 boxes indicate the location of extracted samples for various scenes of clear-sky water (boxes 1–4), clear-sky land (boxes 4–8), ash over water (boxes 9–14), and cloud (boxes 15–28).

at 13:30 UTC over Europe and the Atlantic Ocean where we carefully hand-picked 28 samples representing volcanic ash, cloud, and clear-sky ocean and land surfaces. We do not show a typical dust RGB (e.g., Francis et al., 2012) in Fig. 1 because regions of cloud can be difficult to visually separate from the underlying surface in the dust RGB. Instead, the RGB image in Fig. 1 was produced by assigning the BTD 12.0–10.8 values as the red component, the 0.6 µm reflectance as the green component, and the BTD 10.8–8.7 as the blue component. By using the 0.6 µm channel we could more easily see where small-scale clouds were located over both land and ocean allowing us to pick better samples. Note that we also hand-picked 28 samples on two other days during the Eyjafjallajökull volcanic eruption period, 7 May at 11:00 UTC and 18 May at 16:00 UTC. Overall, we hand-picked 18 samples of ash over water, 6 samples of ash over land, 30 samples of cloud, and 30 samples of clear-sky ocean and land. Figure 2a is a wavelength-versus-reflectivity plot for the three SEVIRI reflectivity channels showing the mean along with minimum and maximum reflectance for the 80 extracted samples; in this figure, the ocean is blue, land is green, ash over water is red, ash over land is pink, ash above cloud is light blue, and cloud is black. Figure 2b is the same as Fig. 2a except wavelength versus temperature for four SEVIRI temperature channels is displayed. For the reflectivity channels, the cloudy samples generally have a much higher reflectivity than the ocean, while the mean reflectivity of ash over water is only about 5–10 % higher than the ocean. However, note the large variation in the reflectance of the cloud and ash samples that make it difficult to use spectral tests alone to separate these features. Nonetheless, in general, the reflectance stays rather constant or increasing for the cloudy samples when moving from the 0.6 to 1.6 µm channels, while the reflectance decreases for the ash over water samples. The mean ash reflectivity drops to only about 6 % at 1.6 µm, mostly due to the fact that ash will typically contain a larger number of smaller particles, which influences a decreasing reflectance from the visible to near-IR wavelengths (Weber et al., 2012). Thus, spectral tests using the difference of two reflectivity channels can be used to better separate features. When analyzing the temperature trend between the 10.8 and 12.0 µm channels in Fig. 2b, the temperature generally increases with wavelength for ash but decreases for the other features, which is due to the unique characteristic of the ash imaginary refractive index being higher at 12.0 than at 10.8 µm causing the slightly lower temperatures at 12.0 µm (Prata, 1989). However, once again a large variation in the temperatures of the various features exists, which makes it difficult to use only spectral tests for developing an accurate classification algorithm. Martins et al. (2002) showed the utility of using spatial (textural) measures to separate aerosols from clouds over oceans due to the mean and standard deviation for a group of aerosol pixels being different than clouds. Spatial measures are a form of texture identification where a group of aerosol pixels appear different than clouds due to several measures, with one example being their homogeneity. Therefore, combining spectral and spatial information reduces the frequency of misclassifications within an image.

In this paper, we take this a step further by using temporal information along with spectral and spatial information as the high temporal resolution of geostationary satellite sensors permits the use of these tests; however only a handful of studies have actually used temporal tests (Calle et al., 2006; de Ruyter de Wildt et al., 2007). Calle et al. (2006) proposed a fire detection technique that utilized temporal information from the 3.9 µm SEVIRI channel and showed that false alarm rates were lower than when detecting fires without using any temporal information. Typically the temperature from the 3.9 µm channel does not encounter large variations with time, but Calle et al. (2006) found that large increases occur with the onset of fires, which helps in the better detection of fires. Cloud detection can also be improved when using temporal information since the temporal variation of the reflectance and temperature of a pixel is usually greatly impacted by the presence of clouds. For example, when analyzing the reflectance of the 0.6 µm SEVIRI channel for a pixel over a period of time, the variation in the reflectance will be minimal in most clear-sky cases but rather large for most cases where clouds are present since clouds are typically much more heterogeneous than the underlying land surface. In the following year, de Ruyter de Wildt et al. (2007) developed temporal tests using reflectance and temperature channels from SEVIRI and found that these tests helped mask clouds and cloud shadows, which ultimately led to more accurate detection of snow cover. Although the temporal tests detected most clouds due to their heterogeneity, they had to rely on the spectral tests to detect the water clouds that were rather homogeneous, since the reflectance and temperature channels showed little temporal variation. Another issue that often arises when using temporal techniques is the overestimation of cloud cover, especially in areas near cloud edges and in areas over broken clouds where a pixel may be cloud-free in the current time step but cloudy in the previous one. This situation can cause a significant increase in the variation

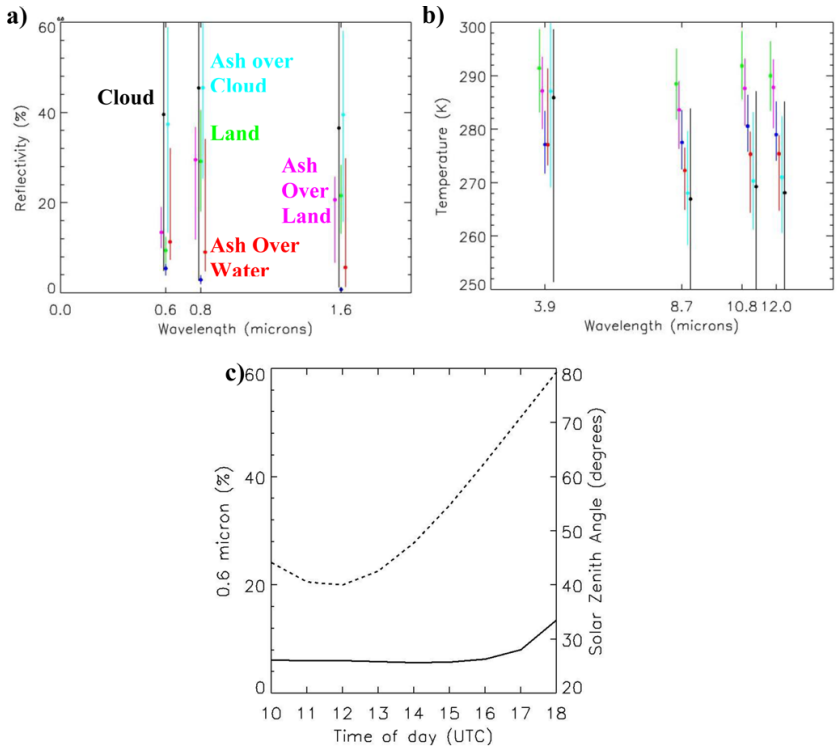

Fig. 2. (a) Wavelength-versus-reflectivity plot for the three SEVIRI reflectivity channels showing the mean along with minimum and maximum reflectance for the 80 extracted samples where the ocean is blue, land is green, ash over water is red, ash over land is pink, ash above cloud is light blue, and cloud is black. **(b)**: same as **(a)** except wavelength versus temperature for four SEVIRI temperature channels is displayed. **(c)** 0.6 µm reflectivity and solar zenith angle for a clear-sky pixel over the water on 5 May 2010 from 10:00 to 18:00 UTC.

of reflectance and temperature with time for a cloud-free pixel. Furthermore, freshly emitted volcanic ash may be detected as cloud when using temporal techniques since the reflectance and temperature of the pixel can vary significantly with time. Therefore, even though temporal techniques have been used successfully for detecting fires and clouds, they also encounter problems; these are investigated further in this study. For instance, freshly emitted volcanic ash plumes can cause large temporal variations

3.1 General flow of algorithm

For our algorithm, we first identify pixels that are land (or over land) and pixels that are water (or over water) to make the algorithm efficient and save computational time. This is necessary since the thresholds used to identify aerosols and clouds are different over water than over land. Classification methods are usually easier over water since water has a low visible reflectance and warmer infrared temperatures when compared to aerosols and clouds. However, over land, spectral tests pose challenges since the surface reflectance and temperatures can be highly variable. After separating land and water pixels, we identify feature pixels through a temporal test over all surfaces along with a spectral test over only water. Feature pixels are simply pixels that are contaminated with any type of aerosol or cloud. Following this, all pixels labeled as feature are fed into the second part of the algorithm, which identifies cloudy pixels through spectral, spatial, and temporal tests. If the feature pixel passes any one of these tests, then it is labeled as cloud. If the pixel fails all of these tests, then the pixel is labeled as aerosol. Since the aerosol spatial distribution maps can be produced every 5 min when using SEVIRI, they can provide near-real-time information on the location of volcanic ash, which is a major aviation concern (Casadevall, 1992). Also, understanding the spatial distribution of aerosol and cloud is very important as this is the first step to accurately quantifying the cloud and aerosol radiative forcing (Kaufman et al., 2002).

3.2 Input data for algorithm

The U.S. Geological Survey (USGS) global land cover characteristics database version 2.0, SEVIRI viewing and solar zenith angles, and the SEVIRI channels highlighted in Table 1 are inputs into our algorithm. SEVIRI viewing and solar zenith angles are primarily used for masking sun glint regions, while the SEVIRI channels provide the critical reflectivity and temperature values for each pixel. The USGS global land cover data are used immediately in the algorithm to separate land and water pixels and to find bright

(e.g., desert) and non-bright (e.g., vegetation) pixels over land since certain threshold tests are not valid over bright surfaces with high reflectivity. Next, we develop a clear-sky reflectance map by finding the minimum top-of-atmosphere (TOA) 0.6 µm reflectance for each pixel over a 14-day period (Jolivet et al., 2008). In order for this algorithm to be used operationally, the 14 days prior to the time of interest are used to find the minimum TOA reflectance for a pixel. For example, if analyzing a 13:00 UTC SEVIRI image on 19 April 2010, then we find the minimum 0.6 µm reflectance from 5 until 19 April at 13:00 UTC for each pixel to generate the clear-sky reflectance map. For bright surfaces determined by the USGS global land cover map, we find the highest 10.8 µm temperature during the 14-day period and then extract the 0.6 µm reflectance from this particular pixel. Dust over desert regions can reduce the observed TOA reflectance below the actual clear-sky reflectance since dust is slightly absorbing at 0.6 µm (Patadia et al., 2009). The use of the 0.6 µm channel means that our algorithm can only be used during the daylight hours, which can be especially problematic at high latitudes during the winter months. Also, the variation in solar zenith angle during the daylight hours can further restrict the time validity of our algorithm. In order to highlight the change in reflectivity that occurs due to the solar zenith angle, we show the 0.6 µm reflectivity for a clear-sky pixel over the water on 5 May 2010 from 10:00 to 18:00 UTC (Fig. 2c). The 0.6 µm reflectivity values remain rather consistent at around 6 % until from 10:00 to 16:00 UTC even though the solar zenith angle varies from 40 to 62°. However, considerable increases in reflectivity occur after 16:00 UTC, especially from 17:00 to 18:00 UTC, when the solar zenith angles are about 70 and 79°, respectively, and the reflectivity of the clear-sky pixel increases from 8 to 13.5 %. Also, our algorithm should not be used when the solar zenith angle is high (i.e., solar zenith angle > 65°) since ash identified by our algorithm will begin converting to cloud. In fact, our algorithm results changed rather drastically when advancing in time from 16:00 to 17:00 UTC for the volcanic ash cases during April and May due to the large increase in reflectivity that occurs when the solar zenith angle is large.

3.3 Algorithm over land

After generating the clear-sky reflectance maps, the algorithm over land begins with a snow detection scheme (not shown in Table 2) so that these bright pixels can be ignored throughout the remainder of the algorithm. This snow detection scheme uses the normalized difference snow index (NDSI), which takes advantage of snow being more reflective at 0.6 µm than at 1.6 µm (Riggs and Hall, 2004), along with other temporal tests. For all the temporal tests used in Table 2, the standard deviation (σ) of three successive 15 min SEVIRI images centered on the current image is computed for the highlighted channels in Table 1. Temporal tests help reduce the frequency of falsely detected clouds as snow (Riggs and Hall, 2004), and for this study we use the σ of the 1.6 and 10.8 µm as the reflectance and temperature of snow generally varies slowly with time (de Ruyter de Wildt et al., 2007). However, we will not go any further into the specifics of the snow detection scheme because it is not critical to the main goal of the algorithm and the results of this paper.

Table 2. Outline of the algorithm applied over land, showing the various thresholds used for the feature tests and cloud tests.

Feature tests
$\lvert 0.6\,\mu m_{CUR} - 0.6\,\mu m_{CLR}\rvert > 1.5\,\%$
Cloud tests
BTD 8.7–10.8 > -2 K and BTD 10.8–12.0 > 0 K
10.8 µm < 240 K and BTD 10.8–12.0 > -0.5 K
1.6 µm > 30 % and BTD 10.8–12.0 > -0.5 K
BTD 10.8–12.0 > 1.5 K
σT 1.6 µm > 1.5 % and BTD 10.8–12.0 > 0 K
$\lvert 0.6\,\mu m_{CUR} - 0.6\,\mu m_{CLR}\rvert > 3.5$ % and BTD 10.8–12.0 > 0 K
σs 1.6 µm > 2.5 % and BTD 10.8–12.0 > 0 K
σs 12.0 µm > 1.5 K and BTD 10.8–12.0 > 0 K

The first test in Table 2 that uses the 0.6 µm clear-sky reflectance maps to determine whether a pixel is a feature is the most important to the success of the algorithm. If the difference between the 0.6 µm reflectance for the current SEVIRI pixel and its clear-sky reflectance is greater than 1.5 % (i.e., $\lvert 0.6\,\mu m_{cur} - 0.6\,\mu m_{clr}\rvert > 1.5$ % in Table 2), then the pixel is classified as a feature. The $0.6\,\mu m_{cur}$–$0.6\,\mu m_{clr}$ test detects features well such as ash for which the 0.6 µm reflectance is typically higher than in clear-sky conditions. Figure 3 shows bispectral plots for the SEVIRI channels of most interest to this study from the samples used to produce Fig. 2. The ocean (blue) and land (green) samples have $0.6\,\mu m_{cur}$–$0.6\,\mu m_{clr}$ values mostly less than 1.5 % (i.e., Fig. 3a). The few land pixels with values slightly higher than 1.5 % are likely due to some cloud contamination occurring within the land samples as the persistent cloud cover over land made it difficult to hand-pick completely clear-sky samples. Nonetheless, there is quite good separation between the clear-sky samples and the atmospheric feature samples when analyzing the $0.6\,\mu m_{cur}$–$0.6\,\mu m_{clr}$ values alone. However, there is some significant overlap between the ash (red and pink) and cloud (black) samples, which is why this test is only used to separate clear-sky and atmospheric feature pixels. Note that we introduce the absolute value in this first test in order to account for scenarios over bright land surfaces where the higher 0.6 µm clear-sky reflectance over these surfaces can completely mask the cloud or aerosol signal. In fact, the presence of an absorbing ash or dust layer over a bright surface can actually reduce the 0.6 µm reflectance below the clear-sky reflectance.

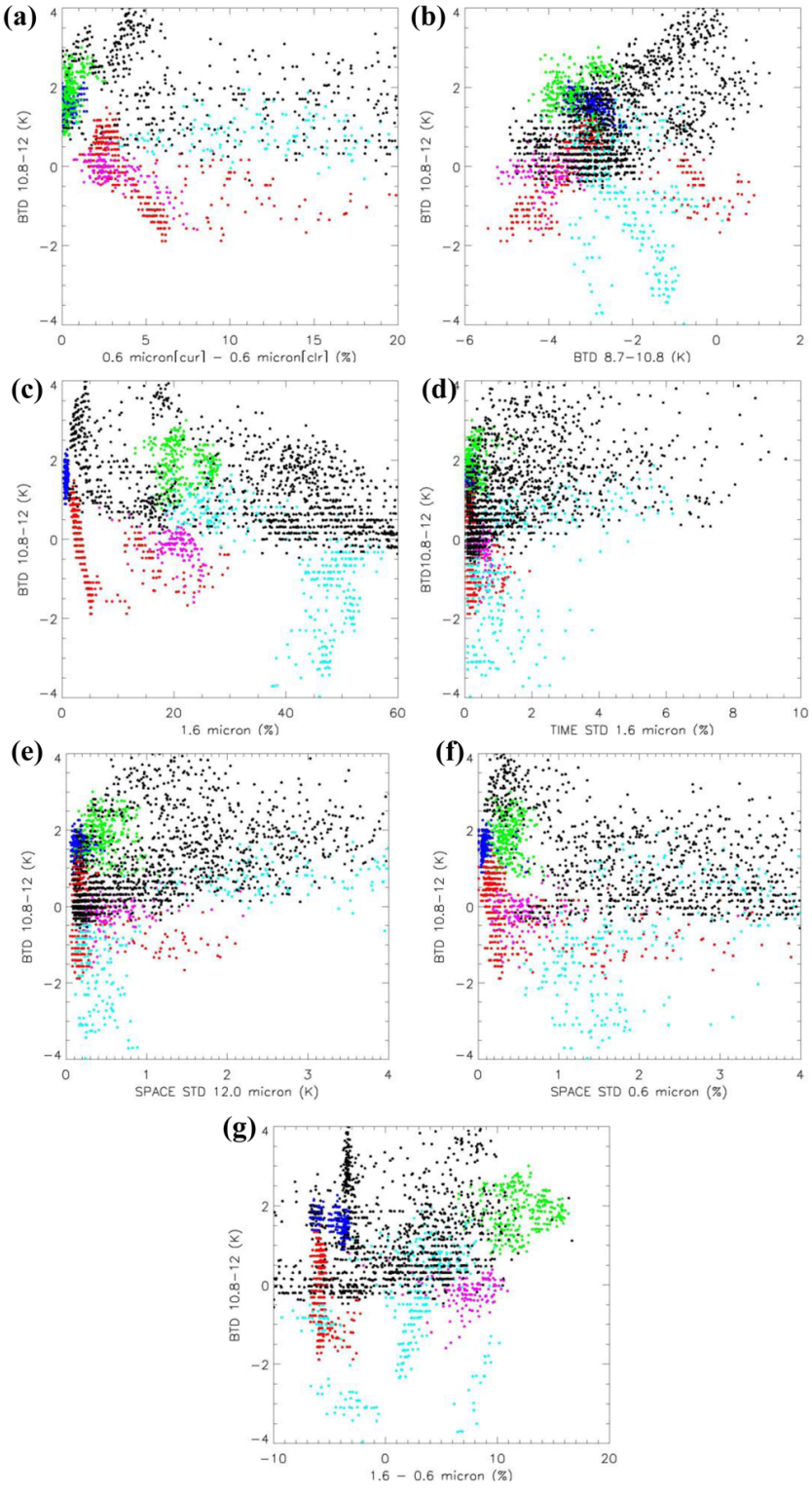

Fig. 3. Bispectral plots for the SEVIRI channels of most interest to this study from the samples in Fig. 2; ocean is blue, land is green, ash over water is red, ash over land is pink, ash above cloud is light blue, and cloud is black. **(a)** 0.6 μm_{cur}–0.6 μm_{clr} versus BTD 10.8–12.0, **(b)** BTD 8.7–10.8 versus BTD 10.8–12.0, **(c)** 1.6 µm versus BTD 10.8–12.0, **(d)** σT 1.6 µm versus BTD 10.8–12.0, **(e)** σs 12.0 µm versus BTD 10.8–12.0, **(e)** σs 0.6 µm versus BTD 10.8–12.0, and **(f)** 1.6 µm–0.6 µm versus BTD 10.8–12.0.

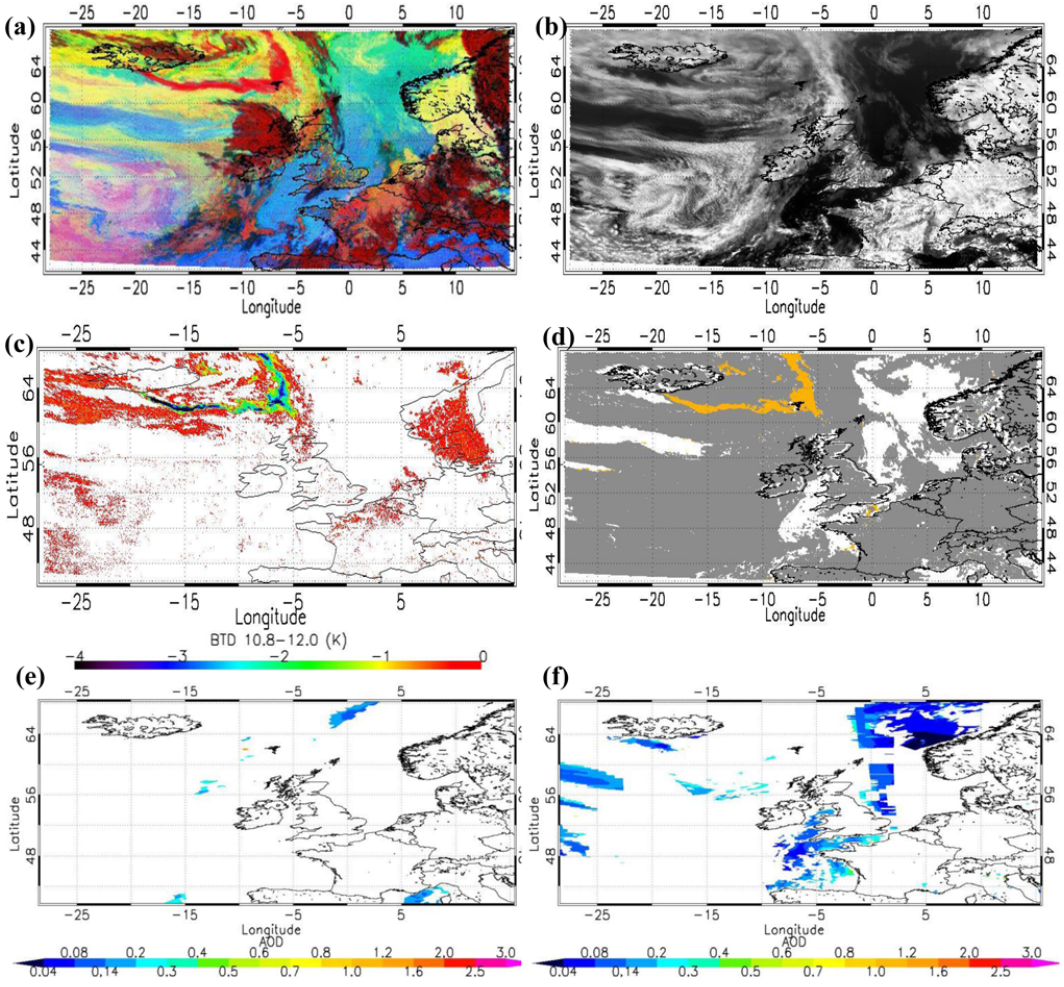

Fig. 4. **(a)** SEVIRI dust RGB image on 13 May 2010 at 12:00 UTC, when a substantial amount of ash was being emitted from the Eyjafjallajökull volcano. The volcanic ash is identified in the SEVIRI RGB image by the reddish colors extending east of Iceland. **(b)** SEVIRI 0.6 µm visible image where clouds appear white against a dark background. **(c)** BTD 10.8–12.0 map. **(d)** Final results of the SEVIRI algorithm, with the pixels labeled as clear sky (white), cloud (gray), and aerosol (orange). **(e)** MODIS Aqua AOD results for 13 May where MODIS pixels with cloud fraction larger than 80 % are removed. **(f)** MISR AOD across the region on this day.

The second test in Table 2 that uses the BTD between the 8.7 and 10.8 µm channels (BTD 8.7–10.8) along with BTD 10.8–12.0 has been shown to detect ice clouds quite accurately (Zhang et al., 2006). Thus, this test is specifically used to detect clouds in our study over all pixels including the feature pixels just detected by the first test. Figure 3b shows that these two tests provide good separation between the various sample types, as the samples with BTD 8.7–10.8 > -2 K and BTD10.8–12.0 > 0 K are nearly all cloud pixels. Ash absorption at 8.7 µm typically helps influence a more negative BTD 8.7–10.8. This is shown in Fig. 3b as many of the fresh, opaque ash clouds (red) have BTD 8.7–10.8 < -4 K, which means that fresh ash will generally not be detected as cloud by this test. Also, note that the ash samples associated with BTD 8.7–10.8 > -2 K have BTD 10.8–12.0 values primarily less than 0 K. Consequently, these will not be identified as cloud by this test. The BTD 8.7–10.8 will vary with ash composition and SO_2 amount in the volcanic cloud, which explains the variation in the values in Fig. 3b. In particular, SO_2 absorption at 8.7 µm leads to a decrease or more negative BTD 8.7–10.8 value. The BTD 10.8–12.0 will vary with ash composition, particle sizes, and atmospheric water vapor content. For example, it is generally more difficult to detect ash in regions of high water vapor content where the BTD 10.8–12.0 may be close to zero or positive.

As the next step, the algorithm separates the feature pixels as cloud or ash by using a series of cloud detection tests. If a feature pixel is not labeled as cloud by the cloud detection tests, then the pixel is labeled as ash. The first cloud detection test labels pixels as cloud when the 10.8 µm < 240 K and BTD 10.8–12.0 > -0.5 K. Freshly emitted volcanic ash can have a temperature that is closely related to its height, so

it is possible that the 10.8 µm temperature can be less than 240 K for ash. Therefore, we also include the BTD 10.8–12.0 µm test since freshly emitted volcanic ash will typically have strongly negative values. Figure 3b shows an example of the strongly negative BTD 10.8–12.0 values that can occur with freshly emitted ash where the fresh ash samples have a BTD 10.8–12.0 µm around −1 K and BTD 8.7–10.8 near 0 K. Then, we apply a test that labels a pixel as cloud if the 1.6 µm > 30 % and BTD 10.8–12.0 > −0.5 K. This study found that even the thickest ash regions will typically have 1.6 µm < 30 % after picking samples of the freshly emitted ash near the Eyjafjallajökull volcano on 7 May. Figure 3c is a scatter plot with the 1.6 µm on the x axis and BTD 10.8–12.0 on the y axis, which clearly shows that all our samples with 1.6 µm > 30 % are cloud contaminated. The next cloud test simply labels the pixel as cloud if the BTD 10.8–12.0 > 1.5 K. Figure 3c shows the utility of this test as ash samples all have BTD 10.8–12.0 < 1.5 K, while the cloudy samples are dominant above this threshold. Thin ash (AOD < 0.2) can have very similar BTD 10.8–12.0 as the land surface since areas of thin ash will have minimal impact on terrestrial radiation. Consequently, thin ash regions can potentially be labeled as cloud by this test but only if the $|0.6\,\mu m_{cur}–0.6\,\mu m_{clr}|$ test labels it as a feature. These thin ash regions do not pose a threat to aviation, so it is not a major issue if thin ash is missed by our algorithm.

The remaining cloud detection tests in Table 2 utilize either spatial or temporal techniques. In this study, the temporal tests take three successive 15 min SEVIRI scans and calculate the σ for each pixel, which is referred to as a σT test throughout the remainder of the paper. We decided to use only three successive SEVIRI images to calculate σ because using more successive images increases the likelihood that both ash and cloud could be included in the σ computation for a pixel where ash and cloud reside nearby, and we want to limit these scenarios as much as possible. Also, by using only three successive images, this algorithm can be used in time-sensitive situations, such as volcanic ash plumes interfering with air traffic, that require real-time decision making. We use a σT tests with the 1.6 µm channel, where the appropriate threshold is chosen based on analyzing the scatter plot in Fig. 3d. All the ash over land samples (pink) were associated with σT 1.6 µm < 1.5 %, while cloudy samples were dominant above this threshold. Ash plumes are generally more homogeneous than clouds, which is the reason for the fairly good separation between ash and cloud samples in Fig. 3d. However, a portion of the cloud samples have very low σT 1.6 µm and cannot be labeled as cloud by this test. The next test in Table 2 uses the $|0.6\,\mu m_{cur}–0.6\,\mu m_{clr}|$ technique along with BTD 10.8–12.0 since we observed good separation between the ash and cloud samples in this multispectral space as revealed by Fig. 3a. This test labels clouds when the $|0.6\,\mu m_{cur}–0.6\,\mu m_{clr}| > 3.5$ % and BTD 10.8–12.0 > 0 K. We include the BTD 10.8–12.0 technique in this test since moderate (AOD > 0.5) and thick (AOD > 1.0) ash regions with BTD 10.8–12.0 < 0 K can have $|0.6\,\mu m_{cur}–0.6\,\mu m_{clr}| > 3.5$ %. Thus, by including the BTD 10.8–12.0 technique the moderate and thick ash plumes will generally not be labeled as cloud. In fact, Fig. 3a shows that as the $|0.6\,\mu m_{cur}–0.6\,\mu m_{clr}|$ increases beyond 3.5 %, the BTD 10.8–12.0 primarily decreases with increasing $|0.6\,\mu m_{cur}–0.6\,\mu m_{clr}|$. Figure 3a suggests that this test can be quite powerful in accurately labeling atmospheric features (e.g., cloud and dust).

The final two tests utilize spatial techniques along with the BTD 10.8–12.0 technique once again. The spatial techniques (i.e., σs tests) compute the σ over a 3×3 pixel region. For the first test, if σs 12.0 µm > 1.5 K and the BTD 10.8–12.0 > 0 K, then the center pixel of the 3×3 pixel group is classified as a cloud. The σs and σT tests work on the similar principles of cloud typically being more heterogeneous than ash except that the σs test operates in space instead of time. This is demonstrated in Fig. 3e, where the cloudy samples tend to have higher σs 12.0 µm values than shown for the ash pixels, but there is considerable overlap between a portion of the cloudy samples and the ash samples. Consequently, we introduce one more spatial test that has the ability to detect many of these cloudy samples that went undetected by the σs 12.0 µm test. This second spatial test labels cloud when the σs 1.2 µm > 1.2 % and BTD 10.8–12.0 > 0 K, and the scatter plot that shows the separation of the various samples in this multispectral space is displayed in Fig. 3f. We see that the cloudy samples that were associated with very low σs 12.0 µm and BTD 10.8–12.0 near 0 K in Fig. 3e are detectable when using the σs 1.6 µm technique. There is more scatter with the ash samples in Fig. 3f, but these ash samples with σs 1.6 µm > 1.2 % have mostly BTD 10.8–12.0 < 0 K, which means that they will not be labeled as cloud by this test. These are likely thick ash plumes (AOD > 1.0) that tend to be more heterogeneous. However, we do notice that a few ash samples will be incorrectly labeled as cloud since they have BTD 10.8–12.0 > 0 K and σs 1.6 µm > 1.2 %. These ash samples were actually taken near the boundaries of thick ash plumes, which means this spatial test can encounter problems due to strong boundaries occurring in SEVIRI imagery. Lastly, the feature pixels that fail all of the final cloud detection tests are labeled as ash. Note that we do show ash above cloud samples (light blue) in the panels in Fig. 3, but we have not discussed them in the preceding paragraphs. The main reason for showing the ash above cloud samples is to stress that it is extremely difficult to separate the ash above cloud from the ash-free cloud samples. One possible way to separate the ash above cloud from the ash-free cloud samples is by using the BTD 10.8–12.0 technique that our algorithm uses in nearly all the tests. Therefore, this algorithm is capable of detecting ash above cloud samples only if the ash influences a negative BTD 10.8–12.0 value. We will show examples of our algorithm detecting ash above cloud in Sect. 4.

Note that our algorithm is capable of detecting all aerosol types that cause an increase in the 0.6 µm clear-sky reflectance values. Consequently, this algorithm should be used along with dust RGB images and other more conventional methods such as the BTD 10.8–12.0 maps during operational situations. Of course, when both ash and dust aerosol are present in a region, then the RGB images and conventional methods will not help separate the aerosol types since both ash and dust generally influence negative BTD 10.8–12.0 values. If our algorithm is used alone in situations where other aerosol types (e.g., smoke) along with ash are present, then aircraft pilots may be falsely alarmed of ash in the area. However, for our particular study period, volcanic ash is the dominant aerosol type throughout the domain, which is why we refer to ash throughout the remainder of the paper.

3.4 Over-water algorithm

We briefly discuss the over-water algorithm since it has many similarities to the over-land algorithm. The only differences between the land and water algorithms are the slightly lower thresholds that are used to detect clouds for the σs 1.6 µm and σs 12 µm techniques and the inclusion of the 1.6 µm–0.6 µm technique. The threshold is lowered to 1 % for the σs 1.6 µm test and 1.0 K for the σs 12 µm test due to the relative homogeneity of the water. The 1.6 µm–0.6 µm test can be quite powerful over the homogeneous water surface, as indicated in Fig. 3g, where 1.6 µm–0.6 µm is on the x axis and the BTD 10.8–12.0 on the y axis. The clear-sky ocean samples (blue) and ash over water samples (red) have very similar 1.6 µm–0.6 µm values ranging mostly from -7 to -3 %. Even the thick ash samples with BTD 10.8–12.0 near -2.0 K have 1.6 µm–0.6 µm values no larger than -3 %. Nevertheless, we include the BTD 10.8–12.0 technique in this test to ensure that thick ash does not get labeled as cloud. The pixel is labeled as cloud by this test when the 1.6 µm–0.6 µm > -2 % and BTD 10.8–12.0 > -1 K. Similar to the over-land algorithm, after applying all the cloud detection tests to the feature pixels, the pixels that fail all the tests and remain as features are labeled as ash.

4 Results and discussion

4.1 13 May 2010 case

Figure 4a is a SEVIRI dust RGB image on 13 April 2010 at 12:00 UTC, when a substantial amount of ash was being emitted from the Eyjafjallajökull volcano. The dust RGB image was produced by assigning the BTD 12.0–10.8 values as the red component, the BTD 10.8–8.7 as the green component, and the BTD 10.8 µm as the blue component (Francis et al., 2012). The volcanic ash is identified in the SEVIRI dust RGB image by the reddish colors extending eastward from Iceland. The visible image shows extensive cloud coverage across the domain, with clouds evident in the location of the volcanic ash plume (i.e., Fig. 4b). This ash plume is primarily associated with BTD 10.8–12.0 < 0 K, with strongly negative values of -4 K within the core of the plume (i.e., Fig. 4c). Note that a substantial amount of pixels not associated with the main ash plume also possess negative BTD 10.8–12.0, as revealed by the reddish colors in Fig. 4c. According to the SEVIRI dust RGB and the visible image, these pixels are primarily cloudy pixels that do not appear to be associated with any ash. For instance, the clouds to the southwest of Iceland have a BTD 10.8–12.0 as low as -0.4 K. The final results of the SEVIRI algorithm are in Fig. 4d, with the pixels labeled as clear sky (white), cloud (gray), and ash (orange). Our algorithm is able to identify the ash plume, even though clouds reside beneath it, since many of the cloud tests in Table 2 include the BTD 10.8–12.0 technique. Also, the ash-free cloudy pixels that were associated with the negative BTD 10.8–12.0 in Fig. 4c are labeled as cloud by our algorithm. Therefore, overall the algorithm performs well for this particular case.

A few pixels are labeled as ash outside of the main ash plume, which we further investigate by analyzing the MISR and MODIS Aqua AOD around the time of interest ($\sim$ 13:00 UTC) on 13 May. Note that MISR has limited spatial coverage due to its limited field of view, but the MISR transect occurring near the center of the domain passes over the eastern section of the ash plume (Fig. 4e). The MISR fails to retrieve any significant area of AOD for the ash plume due to the fact that the retrieval algorithm recognizes the plume as mostly cloud. The MODIS also has difficulty retrieving any AOD for the ash plume due to the extensive cloud coverage in this region. The lack of MISR and MODIS AOD retrievals of the ash plume is not surprising since their algorithms attempt to retrieve AOD for cloud-free regions only. However, the MODIS retrieves AOD where our SEVIRI algorithm labels clear-sky pixels across much of the domain. Much of the MODIS AOD across the domain is less than about 0.15, which suggests that the ash concentrations are very low. Volcanic ash with low concentrations ($< 0.2\,\mathrm{g\,m^{-2}}$) poses no threat to aviation. Therefore, it is not problematic that these areas of low AOD are undetected by our algorithm. Some limited areas of AOD > 0.2 appear just south of Great Britain and southeast of Iceland in the MODIS AOD image, which our algorithm mostly identifies as cloud or clear sky. The fact that some of these areas of AOD > 0.2 reside among clouds, as seen in the SEVIRI dust RGB and visible image, suggest that these may be bad retrievals. For instance, the AOD > 0.2 to the southeast of Iceland is retrieved in a dominantly cloudy region. The retrievals of AOD > 0.2 just south of Great Britain are also occurring either among cloud or adjacent to clouds. It is known that the MODIS AOD tends to have a high bias when the retrievals are adjacent to clouds (Zhang et al., 2006). Nonetheless, a close inspection of the SEVIRI dust RGB implies that some ash may be present just to the south of Great Britain as pinkish colors are shown in this location. The fact that our algorithm labels

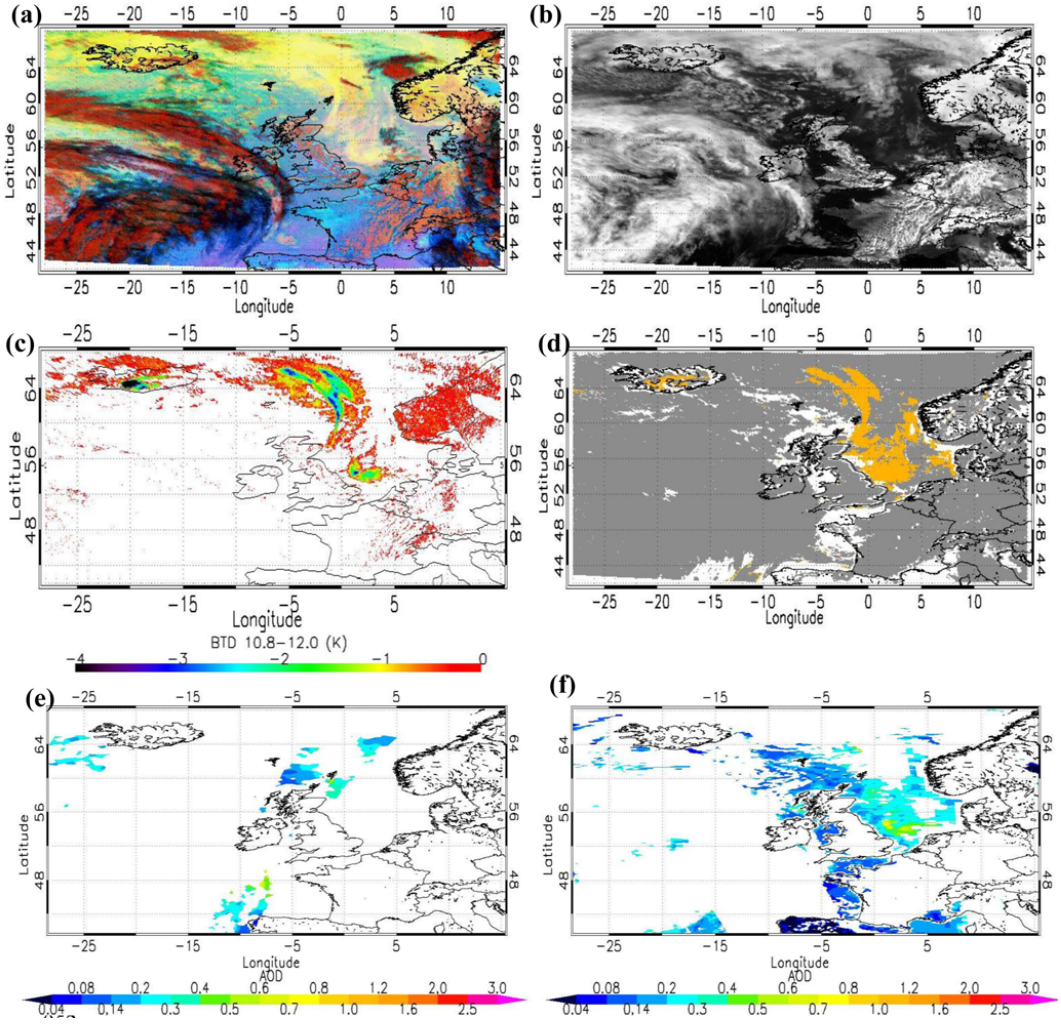

Fig. 5. Panels **(a)**–**(f)** are the same as in Fig. 4 except that this is a SEVIRI RGB image on 17 May 2010 at 13:00 UTC where a significant area of volcanic ash resided over the North Sea around 56° N and 7° W.

some pixels as ash at this same location suggests that the MODIS AOD > 0.2 in this particular region may be real. Figure 4d also reveals that our algorithm may falsely detect ash along cloud edges. These false detections are difficult to see in Fig. 4d, but there are a few occurrences among the cloud edges to the south of Iceland.

4.2 16 and 17 May 2010 case

Figure 5a–f are similar to Fig. 4a–f except that the former pertain to the 17 May 2010 case study at 13:00 UTC, in which a significant area of volcanic ash resided over the North Sea around 56° N and 7° W (Turnbull et al., 2012). This ash plume is not as apparent on the SEVIRI dust RGB due to the fallout of ash particles during its transport from Iceland. In fact, it is difficult to decipher the ash plume from the low-level clouds (yellowish colors) across the domain. Analyzing both the dust RGB and visible image along with the BTD 10.8–12.0 map (i.e., Fig. 5c) helps in better understanding where the potential ash regions are located. The pink to yellow colors associated with the ash plume in the dust RGB appear darker than the whiter clouds in the visible image across the North Sea. By this time, the ash plume has become only slightly more reflective than the background ocean. There are some clouds among the ash plume that are only noticeable when closely inspecting the visible image, which shows the utility of analyzing both the dust RGB and visible image. The BTD 10.8–12.0 map shows a considerable area over the North Sea and Norwegian Sea that has BTD 10.8–12.0 < -1 K, suggesting that concentrated ash is present across the area. Our algorithm is easily able to identify these areas where the BTD 10.8–12.0 < -1 K. According to the dust RGB and visible image, our algorithm successfully disregards cloud-contaminated areas within the ash plume region over the North Sea. For example, clouds are shown off the coast of the Netherlands ($\sim$ 56° N, 5° E) and

this area is labeled as cloud by our algorithm. Overall, our algorithm appears to identify clouds very well across the domain, which is critical as the final ash spatial distribution maps depend on the success of the cloud detection. Moreover, our algorithm identifies ash in locations across the North Sea that have BTD 10.8–12.0 > 0 K and appear to be cloud-free. These results are in fairly good agreement with the spatial distribution of MODIS AOD across the North Sea. MODIS retrieves AOD primarily ranging from 0.2 to 0.4 across the North Sea with the exception of a few higher AOD regions where values near 0.7 are present. The location of the higher AOD regions coincide with BTD 10.8–12.0 < −1 K, while the AOD from 0.2 to 0.4 coincide with near-zero to positive BTD 10.8–12.0 values. The good agreement between the MISR and MODIS AOD in the limited locations of MISR availability over the North Sea and Norwegian Sea gives us better confidence in the accuracy of these satellite retrievals. Although our algorithm is able to detect these areas of optically thinner ash identified by MODIS and MISR, it is likely that they are below the mass concentration threshold of 0.2 g m^{-2} and do not pose a threat to aviation (Francis et al., 2012; Prata and Prata, 2012). Again, our algorithm mostly misses the very low AOD regions below about 0.2 that are detected by MODIS and MISR. For example, our algorithm labels the area just north of Great Britain as clear sky, while the MISR and MODIS retrieves AOD around 0.15. Finally, note that our algorithm is able to detect the thick ash over the Norwegian Sea (∼ 64° N, 0° E) even though it is above a considerable area of clouds according to the SEVIRI visible image. Once again, this shows the ability of our algorithm to detect thick ash above cloud, which can pose a threat to aviation.

The studies of Francis et al. (2012), Prata and Prata (2012), and Marenco et al. (2011) all analyze this 17 May volcanic ash event over the North Sea. Our algorithm detects a much broader area of volcanic ash over the North Sea than shown in Francis et al. (2012) and Prata and Prata (2012). The SEVIRI retrieval algorithms developed in these two studies rely heavily on the BTD 10.8–12.0 approach to detect ash. However, ash is not always associated with BTD 10.8–12.0 < 0 K, especially thinner ash regions (AOD < 0.5). These two studies use FAAM BAe146 aircraft data to validate their results. In particular, Francis et al. (2012) show that their algorithm is able to detect the 17 May ash plume where ash concentrations from the FAAM aircraft are greater than about 0.3 g m^{-2}. However, when FAAM ash concentrations drop below about 0.3 g m^{-2}, their algorithm fails to detect any ash. The FAAM aircraft actually retrieves ash concentrations all the way to the eastern coast of Great Britain, which our algorithm is able to detect (i.e., Fig. 5d). Thus, it appears that our algorithm is capable of detecting more ash compared to the algorithms in Francis et al. (2012) and Prata and Prata (2012). However, the ash areas that are undetected in these two studies have fairly low concentrations (less than about 0.3 g m^{-2}) and may not pose any threat to aviation. Marenco et al. (2011) perform modeling simulations of this volcanic ash event where the model shows a broad area of ash over the North Sea. In fact, the area of ash simulated by the model is even larger than the broad area identified by our algorithm.

The FAAM BAe146 aircraft flights on 16 and 17 May are very helpful for verifying the proposed SEVIRI algorithm (Marenco et al., 2011). Figure 6c is a SEVIRI RGB image on 16 May at 15:00 UTC where the BAe146 aircraft took off in southeastern England (52.1° N, 0.3° W) at approximately 12:55 UTC and landed in northwestern France (47.7° N, 2.1° W) at about 18:10 UTC. A nearest-pixel approach is used to collocate SEVIRI to the BAe146 aircraft in space while we find the closest SEVIRI overpass time to each point along the BAe146 aircraft track to collocate in time. Thus, 15 min SEVIRI scans beginning 11:30 UTC and ending 17:00 UTC were used to produce Fig. 6a and b even though only the 15:00 UTC SEVIRI RGB imagery is in Fig. 6c.

The aircraft flight began in cloudy conditions across southeastern England and then headed northwest into an ash plume with scattered clouds as shown by Fig. 6c, where the ash is highlighted by the pinkish colors and clouds by the green and yellowish colors. Since clouds were the dominant feature in southern England, AOD was not reported, but as the aircraft tracked northwestward, the AOD jumped to about 0.2 until thick ash was measured at about 55° N and 4.3° W with an AOD of nearly 0.9 (i.e., Fig. 6a). The SEVIRI algorithm accurately classifies clouds in southern England, but then classifies a mix of clear skies, clouds, and ash where the low AOD of 0.2 is measured, which again suggests that the SEVIRI algorithm has uncertainties in detecting optically thin ash regions. However, Fig. 6b shows several significant increases in 0.6 µm reflectivity in the low AOD region, which hints at cloud contamination. Furthermore, the ash extinction coefficient profiles from the BAe146 aircraft on 16 May shown in Marenco et al. (2011) reveal some low-level clouds in the low AOD region, which suggests the SEVIRI algorithm is classifying clouds properly in this region. When the AOD reaches nearly 0.9, the SEVIRI algorithm classifies nearly all ash pixels adequately except for a few pixels that are associated with 0.6 µm > 40 %, indicating possible cloud contamination. The ash extinction coefficient profiles in Marenco et al. (2011) also indicate low-level cloud contamination below the thick ash. Thus, according to the BAe146 aircraft data, the SEVIRI algorithm is accurate in labeling a few cloud pixels among the ash. Then, another region of low AOD is measured by the aircraft before flying over thicker ash around 55.2° N and 3.9° W with an AOD of about 0.7. The ash is almost entirely missed by the SEVIRI algorithm in this low AOD region as the algorithm classifies mostly clouds. However, the significant increases in 0.6 µm reflectivity among the low AOD region indicates that clouds are present along the aircraft transect. In Marenco et al. (2011), low-level clouds are revealed all along this section

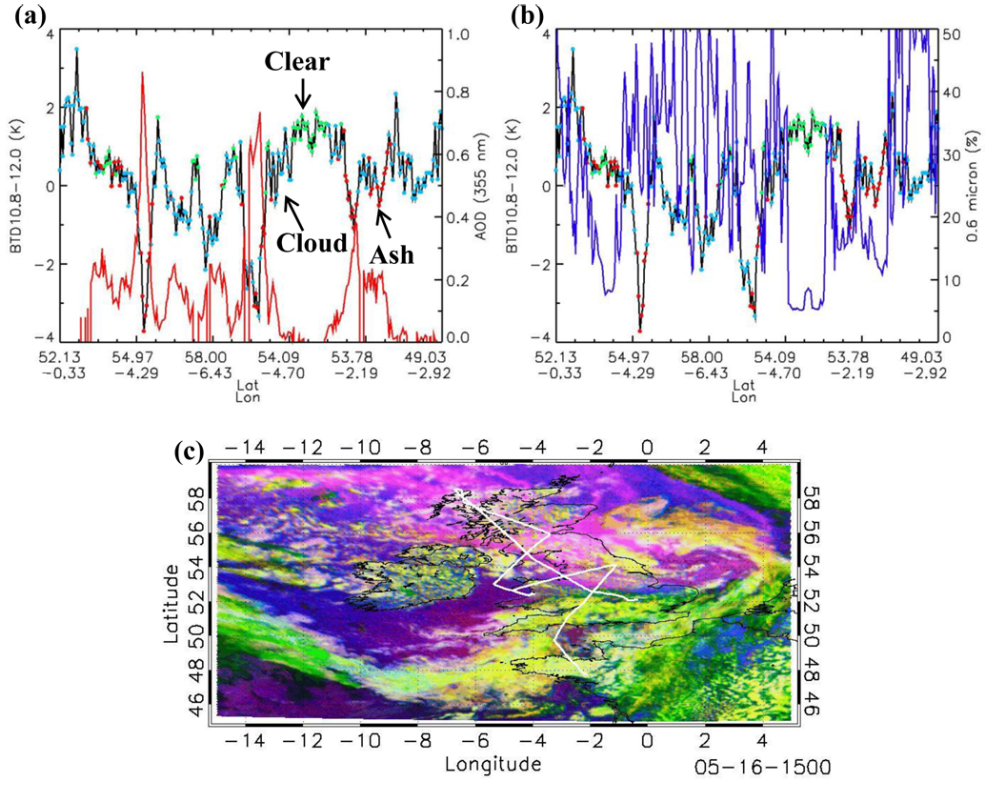

Fig. 6. (a) 355 nm AOD from the BAe146 aircraft in red with the corresponding AOD scale on the right *y* axis and SEVIRI BTD 10.8–12.0 in black with its scale on the left *y* axis. The dots along the black line indicate the results from the SEVIRI algorithm along the aircraft flight, with green, blue, and red denoting clear, cloud, and aerosol, respectively. **(b)** SEVIRI BTD 10.8–12.0, again in black, along with 0.6 µm reflectivity in blue with its scale on the *y* axis from 0 to 50 %. **(c)** SEVIRI RGB image on 16 May at 15:00 UTC with the intricate BAe146 aircraft flight track shown in white.

of the BAe146 flight track, further hinting at the accuracy of the SEVIRI algorithm. The algorithm classifies some ash pixels in the higher AOD region, but clouds are classified more frequently here as the 0.6 µm reflectivity has a significant increase near the minimum in BTD10.8–12.0, indicating the presence of clouds among the thick ash. Also, fairly thick, lower-level clouds are shown along the ash extinction profiles in Marenco et al. (2011) with this thicker ash region. Next, the aircraft encounters very thin ash along its track as AOD drops to near-zero values. As expected the SEVIRI algorithm fails to detect any of this ash and classifies mostly clear skies along this portion of the aircraft track. The aircraft flies over one more noteworthy ash region as AOD jumps to about 0.4 and then quickly drops to 0.2 at about 53.8° N and 2.2° W. The ash associated with the AOD of 0.4 is successfully detected by the algorithm, which appears to be cloud-free from analyzing the 0.6 µm reflectivity and ash extinction profiles in Marenco et al. (2011). However, as soon as the AOD decreases, clouds become an issue once again as the 0.6 µm reflectivity jumps to about 35 %.

The 17 May BAe146 aircraft flight is overlaid in white on the SEVIRI RGB image from 14:00 UTC on that same day in Fig. 7c. However, for this flight, the aircraft started in northwestern France at 11:26 UTC and landed in southeastern England at 16:58 UTC. As seen in the RGB image, the aircraft encountered the main ash plume over the North Sea, while scattered clouds impacted the flight over England and Scotland. Figure 7a and b are the same as Fig. 6a and b except the aircraft AOD and SEVIRI measurements from 17 May are shown. The times when the aircraft were above the scattered clouds over land are clearly seen in Fig. 7b by the very significant increases in 0.6 µm reflectivity, and the SEVIRI algorithm successfully classifies these regions as cloud. After the first period of scattered clouds over land, the aircraft flies over ocean (∼ 53° N, 2.5° W) before making a west-to-east path over land. When the aircraft is over the ocean, the SEVIRI algorithm classifies mostly clear skies with a mix of some cloud and ash. At this time, 355 nm AOD from the aircraft is very low, with most values being less than 0.1, which suggests the SEVIRI algorithm has difficulty detecting ash over water when the AOD is < 0.1. The aircraft measures AOD near 0.2 during its brief west–east transect over land, but the SEVIRI algorithm classifies cloud in this region, and the algorithm appears to be correct according to the strong peak in 0.6 µm reflectivity and the BAe146 ash extinction profiles along this section of the aircraft track in Marenco et

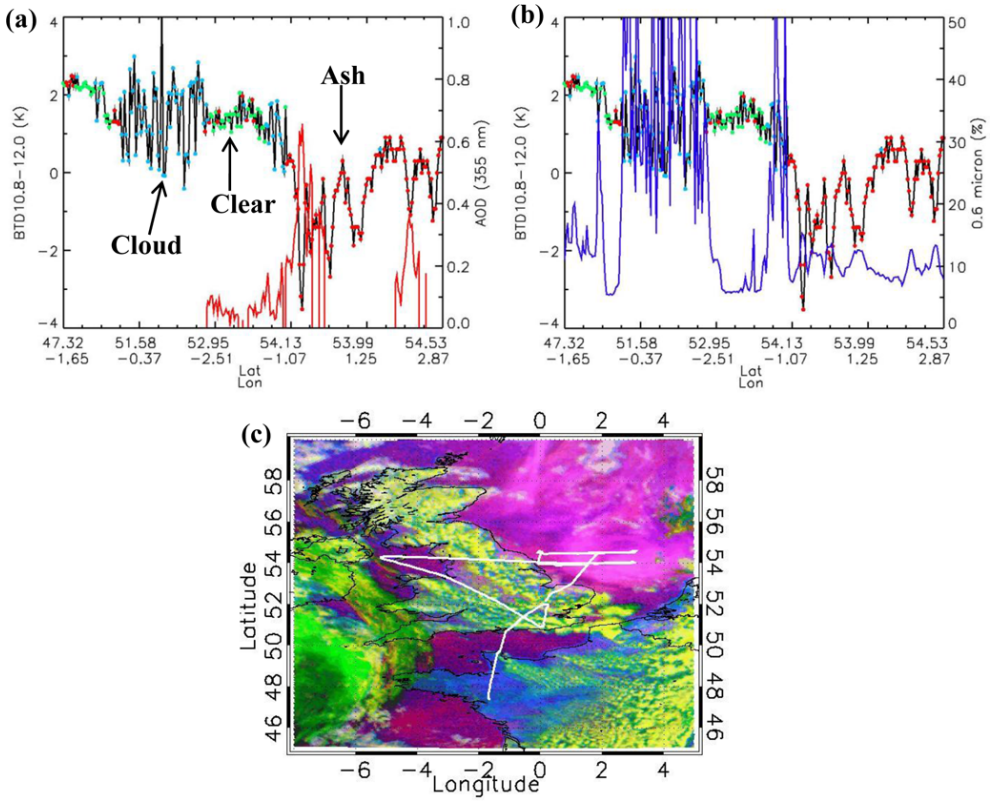

Fig. 7. Panels **(a)** and **(b)** are the same as panels **(a)** and **(b)** in Fig. 6 except the aircraft AOD and SEVIRI measurements from 17 May are shown here. **(c)** The 17 May BAe146 aircraft flight is overlaid in white on the SEVIRI RGB image from 14:00 UTC; for this flight, the aircraft took off in northwestern France at 11:26 UTC and landed in southeastern England at 16:58 UTC.

al. (2011). After traversing land, the aircraft immediately encounters the main ash plume when flying over the North Sea as indicated by the large increase in 355 nm AOD to about 0.6 in Fig. 7a. Then, the descent of the aircraft beneath the ash plume explains the sudden decrease of AOD to zero while the SEVIRI algorithm still detects ash. When the aircraft ascends, it measures the ash plume again as the AOD increases to nearly 0.4 before descending and measuring zero AOD the remainder of its flight path. From analyzing the SEVIRI 0.6 µm reflectivity along with the SEVIRI RGB image, it appears that cloud contamination is minimal across the main ash plume region. Thus, the algorithm performs very well over the ash plume region as only one cloud pixel is detected amongst the ash pixels.

4.3 Validation experiment

In order to obtain a better understanding of the accuracy of our SEVIRI algorithm, we perform an additional experiment where we choose 28 samples for three different days and times (i.e., 7 May at 11:00 UTC, 11 May at 13:00 UTC, and 18 May at 16:00 UTC) during the Eyjafjallajökull volcanic eruption period. These "truth" samples were chosen by examining the dust RGB images along with visible and infrared images and carefully picking areas of clear sky, volcanic ash, and clouds. Note that these samples are different from the ones chosen in Sect. 3 to produce the scatter plots in Figs. 2 and 3. Then, we run our algorithm for these three different days and check the results against the "truth" samples. An example of the 28 samples chosen for the 7 May at 11:00 UTC case is shown in Fig. 8a, where boxes 1–4 are clear-sky ocean, 5–12 are volcanic ash, and 13–28 are clouds. We had very limited clear-sky land pixels available on this day, which explains why we did not choose any samples of clear-sky land. The 84 samples taken on these three days represent the truth. Then, we run our SEVIRI algorithm for these three cases and compare the results against truth samples. Overall, we picked 30 ash over water samples on these three days, which gave a total of 1080 individual ash pixels to compare against our algorithm results as the size of the each sample spanned 6×6 boxes. According to the truth samples, the algorithm performed very well as 936 of the 1080 pixels were accurately labeled as ash by our algorithm, giving a success rate of 87 %. Not surprisingly, our algorithm performed even better in identifying clouds. Overall, the 60 samples of clouds that we picked provided us with 2160 individual cloud pixels as truth. Our algorithm successfully labeled 2127 of these truth pixels as cloud, which gives

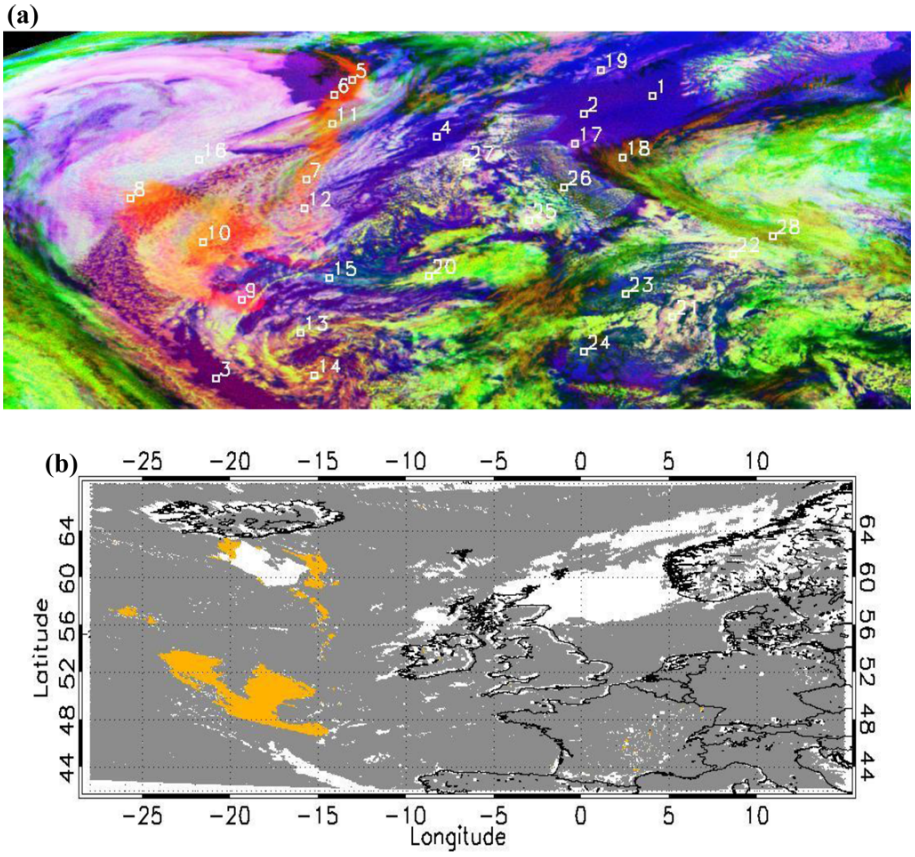

Fig. 8. (a) SEVIRI RGB image on 7 May 2010 at 11:00 UTC over Europe and the Atlantic Ocean; the 28 boxes indicate the location of extracted samples for various scenes of clear-sky water (boxes 1–4), ash above cloud (boxes 5–12), and ash-free cloud (boxes 13–28). **(b)** SEVIRI algorithm results for this 7 May case.

a 98 % success rate for cloud identification. Of course, when performing a validation experiment where we are carefully hand-picking "truth" samples, it is easy to make an algorithm appear more accurate than reality by choosing samples that should be easy for the algorithm to handle. For this validation experiment, we chose samples that, in our opinion, have a wide range of difficulty for the algorithm to identify. Finally, we present the SEVIRI algorithm results for the 7 May at 11:00 UTC case, where the majority of the ash plume is accurately labeled by the algorithm. This is another case where ash resided above clouds, which can make it difficult to identify the ash due to the presence of the cloud. In fact, our algorithm is not able to identify the full extent of the ash plume since the BTD 10.8–12.0 values increase to near or above 0 K. As a result, our algorithm recognizes parts of the ash plume as cloud.

5 Conclusions

In this study we have developed a unique algorithm combining spectral, spatial, and temporal threshold tests using SEVIRI measurements to separate between clear skies, clouds, and ash. We focus on the Eyjafjallajökull volcanic eruption period during April and May 2010, when a substantial amount of ash was transported from the volcano to over the North Sea and Europe. Aerosol (e.g. ash) spatial distribution maps were generated every hour during the daytime beginning with the initial eruption on 14 April and ending on 23 May. In this paper we focus specifically on the daytime volcanic ash cases on 13, 16, and 17 May, when numerous sources of validation data were available. By using MODIS, MISR, and BAe146 aircraft data as verification data, we show that the algorithm is capable of generating accurate ash spatial distribution maps for solar zenith angles $< 65°$. First, the SEVIRI ash spatial distribution maps show important similarities to the MODIS and MISR AOD products, which suggests that the proposed algorithm works well. Second, the BAe146 aircraft shows that the SEVIRI algorithm detects nearly all ash regions over both land and water when AOD > 0.2. However, the MODIS, MISR, and BAe146 aircraft data suggest that the algorithm may encounter some problems detecting ash when AOD < 0.1 over water and AOD < 0.2 over land. Also, our algorithm should not be used when the solar zenith angle is high (i.e., solar

zenith angle > 65°) since ash identified by our algorithm will begin converting to cloud. Another major limitation of this algorithm is that it can only be applied during daytime, and for these high-latitude regions, daytime hours can be severely limited.

Since the damaging effects of volcanic ash to commercial airplanes can be life threatening, accurately tracking ash during volcanic eruption periods is vital. Polar-orbiting satellite sensors do not have the temporal resolution to effectively track volcanic ash. Thus, geostationary sensors, such as SEVIRI, are absolutely critical for tracking volcanic ash and ensuring the safety of passengers onboard commercial airplanes. The accurate ash spatial distribution maps, which can be generated every 15 min by the proposed SEVIRI algorithm, can serve as an extremely important tool during volcanic eruptions.

Acknowledgements. This research is sponsored by NASA's Radiation Sciences as well as ACMAP programs. Special thanks to Jim Haywood, Ben Johnson, and Franco Marenco for the aircraft data used in this paper. The authors thank the anonymous reviewers for their helpful and constructive comments that helped improve the manuscript.

Edited by: O. Torres

References

Ackerman, S. A., Holz, R. E., Frey, R., Eloranta, E. W., Maddux, B. C., and McGill, M.: Cloud detection with MODIS. Part II: Validation, J. Atmos. Ocean. Technol., 25, 1073–1086, 2008.

Ansmann, A., Tesche, M., Groß, S., Freudenthaler, V., Seifert, P., Hiebsch, A., Schmidt, J., Wandinger, U., Mattis, I., Müller, D., and Wiegner, M.: The 16 April 2010 major volcanic ash plume over central Europe: EARLINET lidar and AERONET photometer observations at Leipzig and Munich, Germany, Geophys. Res. Lett., 37, L13810, doi:10.1029/2010GL043809, 2010.

Ansmann, A., Tesche, M., Seifert, P., Groß, S., Freudenthaler, V., Apituley, A., Wilson, K. M., Serikov, I., Linné, H., Heinold, B., Hiebsch, A., Schnell, F., Schmidt, J., Mattis, I., Wandinger, U., and Wiegner, M.: Ash and fine-mode particle mass profiles from EARLINET-AERONET observations over central Europe after the eruptions of the Eyjafjallajökull volcano in 2010, J. Geophys. Res., 116, D00U02, doi:10.1029/2010JD015567, 2011.

Calle, A., Casanova, J. L., and Romo, A.: Fire detection and monitoring using MSG Spinning Enhanced Visible and Infrared Imager (SEVIRI) data, J. Geophys. Res., 111, G04S06, doi:10.1029/2005JG000116, 2006.

Casadevall, T. J.: Volcanic hazards and aviation safety. Lessons from the past decade, 210–220, 1992.

Christopher, S. A. and Wang, J.: Intercomparison between multi-angle imaging spectroradiometer (MISR) and sunphotometer aerosol optical thickness in dust source regions over China: implications for satellite aerosol retrievals and radiative forcing calculations, Tellus Ser. B-Chemical and Physical Meteorology, 56, 451–456, 2004.

Christopher, S. A., Johnson, B., Jones, T. A., and Haywood, J.: Vertical and spatial distribution of dust from aircraft and satellite measurements during the GERBILS field campaign, Geophys. Res. Lett., 36, L06806, doi:10.1029/2008gl037033, 2009.

Christopher, S. A., Feng, N., Naeger, A. R., Johnson, B. T. T., and Marenco, F.: Satellite Remote Sensing Analysis of the 2010 Eyjafjallajokull Volcanic Ash Cloud over the North Sea during May 4–May 18, 2010, J. Geophys. Res, 117, D00U20, doi:10.1029/2011JD016850, 2012.

Diner, D. J., Abdou, W. A., Ackerman, T. P., Crean, K., Gordon, H. R., Kahn, R. A., Martonchik, J. V., McMuldrock S., Paradise, S. R., Pinty, B., Verstraete, M. M., Wang, M., and West R.: Level 2 Aerosol Retrieval Algorithm Theoretical Basis, Rep. D11400, Rev. D, Jet Propulsion Laboratory, Pasadena, California, 1999.

de Ruyter de Wildt, M., Seiz, G., and Gruen, A.: Operational snow mapping using multitemporal Meteosat SEVIRI imagery, Remote Sens. Environ., 109, 29–41, 2007.

Francis, P. N., Cooke, M. C., and Saunders, R. W.: Retrieval of physical properties of volcanic ash using Meteosat: A case study from the 2010 Eyjafjallajökull eruption, J. Geophys. Res., 117, D00U09, doi:10.1029/2011JD016788, 2012.

Gudmundsson, M. T., Thordarson, T., Höskuldsson, A., Gudrún, L., Björnsson, H., Prata, F. J., Oddsson, B., Magnússon, E., Högnadóttir, T., Petersen, G. N., Hayward, C. L., Stevenson, J. A., and Jónsdóttir, I.: Ash generation and distribution from the April–May 2010 eruption of Eyjafjallajökull, Iceland, Sci. Rep. 2, 572, doi:10.1038/srep00572, 2012.

Hsu, N. C., Si-Chee, T., King, M. D., and Herman, J. R.: Deep Blue Retrievals of Asian Aerosol Properties During ACE-Asia, Geosci. Remote Sens., 44, 3180–3195, 2006.

Johnson, B., Turnbull, K., Brown, P., Burgess, R., Dorsey, J., Baran, A. J., Webster, H., Haywood, J., Cotton, R., Ulanowski, Z., Hesse, E., Woolley, A., and Rosenberg, P.: In situ observations of volcanic ash clouds from the FAAM aircraft during the eruption of Eyjafjallajökull in 2010, J. Geophys. Res. Atmos., 117, D00U24, doi:10.1029/2011JD016760, 2012.

Jolivet, D., Ramon, D., Bernard, E., Deschamps, P.-Y., Riedi, J., Nicolas, J.-M., and Hagolle, O.: Aerosol monitoring over land using MSG/SEVIRI. EUMETSAT Meteorological Satellite Conference, Darmstadt, Germany, 8–12 September, 2008.

Kahn, R. A., Gaitley, B. J., Martonchik, J. V., Diner, D. J., Crean, K. A., and Holben, B.: Multiangle Imaging Spectroradiometer (MISR) global aerosol optical depth validation based on 2 years of coincident Aerosol Robotic Network (AERONET) observations, J. Geophys. Res., 110, D10S04, doi:10.1029/2004jd004706, 2005.

Kaufman, Y. J., Tanre, D., and Boucher, O.: A satellite view of aerosols in the climate system, Nature, 419, 215–223, 2002.

Krotkov, N. A., Torres, O., Seftor, C., Krueger, A. J., Kostinski, A., Rose, W. I., Bluth, G. J. S., Schneider, D., and Schaefer, S. J.: Comparison of TOMS and AVHRR Volcanic Ash Retrievals from the August 1992 Eruption of Mt. Spurr, Geophys. Res. Lett., 26, 455–458, 1999.

Marenco, F., Johnson, B., Turnbull, K., Newman, S., Haywood, J., Webster, H., and Ricketts, H.: Airborne lidar observations of the 2010 Eyjafjallajkull volcanic ash plume, J. Geophys. Res. Atmos., 116, D00U05, doi:10.1029/2011JD016396, 2011.

Martins, J. V., Tanré, D., Remer, L., Kaufman, Y., Mattoo, S., and Levy, R.: MODIS cloud screening for remote sensing of aerosols

over oceans using spatial variability, Geophys. Res. Lett., 29, 4-1–4-4, 2002.

Martonchik, J. V., Diner, D. J., Kahn, R. A., Ackerman, T. P., Verstraete, M. M., Pinty, B., and Gordon, H. R.: Techniques for the retrieval of aerosol properties over land and ocean using multiangle imaging, Geosci. Remote Sens., 36, 1212–1227, 1998.

Millington, S. C., Saunders, R. W., Francis, P. N., and Webster, H. N.: Simulated volcanic ash imagery: A method to compare NAME ash concentration forecasts with SEVIRI imagery for the Eyjafjallajkull eruption in 2010, J. Geophys. Res. Atmos., 117, D00U17, doi:10.1029/2011JD016770, 2012.

Naeger, A. R., Christopher, S. A., Ferrare, R., and Liu, Z.: A new technique using infrared satellite measurements to improve the accuracy of the CALIPSO cloud-aerosol discrimination method, Trans. Geosci. Remote Sens., 51, 642–653, 2013.

Patadia, F., Yang, E.-S., and Christopher, S. A.: Does dust change the clear sky top of atmosphere shortwave flux over high surface reflectance regions?, Geophys. Res. Lett., 36, L15825, doi:10.1029/2009gl039092, 2009.

Pavolonis, M. J., Feltz, W. F., Heidinger, A. K., and Gallina, G. M.: A daytime complement to the reverse absorption technique for improved automated detection of volcanic ash, J. Atmos. Ocean. Technol., 23, 1422–1444, 2006.

Pergola, N., Tramutoli, V., Marchese, F., Scaffidi, I., and Lacava, T.: Improving volcanic ash cloud detection by a robust satellite technique, Remote Sens. Environ., 90, 1–22, 2004.

Prata, A. J.: Infrared radiative transfer calculations for volcanic ash clouds, Geophys. Res. Lett., 16, 1293–1296, 1989.

Prata, A. J. and Kerkmann, J.: Simultaneous retrieval of volcanic ash and SO2 using MSG-SEVIRI measurements, Geophys. Res. Lett., 34, L05813, doi:10.1029/2006GL028691, 2007.

Prata, A. J. and Prata, A. T.: Eyjafjallajökull volcanic ash concentrations determined using Spin Enhanced Visible and Infrared Imager measurements, J. Geophys. Res., 117, D00U23, doi:10.1029/2011JD016800, 2012.

Prata, F., Bluth, G., Rose, B., Schneider, D., and Tupper, A.: Comments on "Failures in detecting volcanic ash from a satellite-based technique", Remote Sens. Environ., 78, 341–346, 2001.

Remer, L. A., Kaufman, Y. J., Tanré, D., Mattoo, S., Chu, D. A., Martins, J. V., Li, R.-R., Ichoku, C., Levy, R. C., Kleidman, R. G., Eck, T. F., Vermote, E., and Holben, B. N.: The MODIS Aerosol Algorithm, Products, and Validation, J. Atmos. Sci., 62, 947–973, doi:10.1175/JAS3385.1, 2005.

Riggs, G. A. and Hall, D. K.: Snow Mapping with the MODIS Aqua Instrument, 61st Eastern Snow Conference, Portland, Maine, 9–11 June 2004, 81–84, 2011.

Saunders, R. W. and Kriebel, K. T.: An improved method for detecting clear sky and cloudy radiances from AVHRR data (North Atlantic), Int. J. Remote Sens., 9, 123–150, 1988.

Savtchenko, A., Ouzounov, D., Ahmad, S., Acker, J., Leptoukh, G., Koziana, I., and Nickless D.: Terra and Aqua MODIS products available from NASA GES DAAC, Adv. Space Res., 34, 710–714, 2004.

Schmetz, J., Pili, P., Tjemkes, S., Just, D., Kerkmann, J., Rota, S., and Ratier, A.: An Introduction to Meteosat Second Generation (MSG), B. Am. Meteorol. Soc., 83, 977–992, doi:10.1175/1520-0477(2002)083<0977:AITMSG>2.3.CO;2, 2002.

Seftor, C. J., Hsu, N. C., Herman, J. R., Bhartia, P. K., Torres, O., Rose, W. I., Schneider, D. J., and Krotkov, N.: Detection of volcanic ash clouds from Nimbus 7/total ozone mapping spectrometer, J. Geophys. Res., 102, 16749–16759, doi:10.1029/97JD00925, 1997.

Sigmundsson, F., Hreinsdóttir, S., Hooper, A., Árnadóttir, T., Pedersen, R., Roberts, M. J., Óskarsson, N., Auriac, A., Decriem, J., Einarsson, P., Geirsson, H., Hensch, M., Ófeigsson, B. G., Sturkell, E., Sveinbjörnsson, H., and Feigl, K. L.: Intrusion triggering of the 2010 Eyjafjallajökull explosive eruption, Nature, 468, 426–432, 2010.

Turnbull, K., Johnson, B., Marenco, F., Haywood, J., Minikin, A., Weinzierl, B., Schlager, H., Schumann, U., Leadbetter, S., and Woolley, A.: A case study of observations of volcanic ash from the Eyjafjallajökull eruption: 1. in situ airborne observations, J. Geophys. Res. Atmos., 117, D00U12, doi:10.1029/2011JD016688, 2012.

Weber, K., Eliasson, J., Vogel, A., Fischer, C., Pohl, T., van Haren, G., Meier, M., Grobéty, B., and Dahmann, D.: Airborne in-situ investigations of the Eyjafjallajökull volcanic ash plume on iceland and over north-western Germany with light aircrafts and optical particle counters, Atmos. Environ., 48, 9–21, 2012.

Zhang, P., Lu, N. M., Hu, X. Q., and Dong, C. H.: Identification and physical retrieval of dust storm using three MODIS thermal IR channels, Global Planet. Change, 52, 197–206, 2006.